Computers and Geotechnics 188 (2025) 107537

Contents lists available at ScienceDirect

Computers and Geotechnics

journal homepage: www.elsevier.com/locate/compgeo

Research paper

Large deformation simulations of structure–soil-interaction in anisotropic fine-grained soils

D.A. Dao [a,*], M. Tafili [b], F. Williams-Riquer [a], J. Grabe [a], T. Wichtmann [b]

[a] Institute of Geotechnical Engineering and Construction Management, Hamburg University of Technology, Schellerdamm 22, Hamburg, 21079, Germany
[b] Chair of Soil Mechanics, Foundation Engineering and Environmental Geotechnics, Ruhr-Universität Bochum, Universitätsstraße 150, Bochum, 44801, North Rhine-Westphalia, Germany

ARTICLE INFO

Keywords:
CEL
Pile penetration
Soil–structure-interaction
Clay
Fine-grained soils
Crane stability
Large deformations
LDFE
AVISA
OCR
Anisotropy
Dynamics

ABSTRACT

Structure–soil-interaction in fine-grained soils is strongly influenced by rate dependency, anisotropy, and overconsolidation effects. While advanced constitutive models such as Anisotropic Visco-Intergranular Strain Anisotropy (AVISA) can capture the fine-grained soil effects, the model application is typically limited to small strain problems due to numerical challenges. This study presents the first successful implementation of the AVISA model within explicit simulations in Abaqus, enabling robust modelling of large deformation problems in fine-grained soils. Two previously underexplored applications are investigated: (i) the stability assessment of a Liebherr LTR 1220 telescopic crawler crane during dynamic uppercarriage rotation under varying overconsolidation ratios (OCR), and (ii) the penetration process of an open-ended tubular pile in anisotropic, overconsolidated clay, focusing on penetration resistance and the evolution of stress and void ratio. Both problems are simulated using the Lagrangian FEM and the Coupled Eulerian–Lagrangian (CEL) approach and are qualitatively compared to available field data. The results demonstrate the capability of the AVISA model to address complex large deformation geotechnical problems realistically. The proposed approach provides new insights and practical tools for modelling structure–soil-interaction in situations where conventional methods often fail.

1. Introduction

While accurate modelling of large displacements and dynamic effects is essential in geotechnical engineering, conventional small strain finite element methods (FEM) are prone to excessive mesh distortion and loss of accuracy under extreme deformation.

Traditionally, many constitutive models for clays have been developed under the assumption of isotropy, where the mechanical behaviour is considered uniform in all directions. These models, such as the Modified Cam Clay model (Roscoe and Burland, 1968) and its variants (Zouain et al., 2010; Zhou et al., 2022; Mita et al., 2004), have been widely used because of their relative simplicity and ability to capture the essential features of clay behaviour under various stress paths (Fourie and Potts, 1991; Zdravković et al., 2020; Miranda et al., 2020; Tafili et al., 2024c).

However, natural clays often exhibit inherent anisotropy, stemming from their depositional history, sedimentation, and subsequent geological processes. This inherent anisotropy affects stiffness (Graham and Houlsby, 1983; Wichtmann and Triantafyllidis, 2018), strength (Gylland et al., 2014; Tafili et al., 2023a), and deformation characteristics (Rødvand et al., 2023; Tafili et al., 2021b), leading to directional dependence of mechanical response even before any loading is applied (Andersen et al., 1993; Tafili and Triantafyllidis, 2023; Tafili et al., 2021a; Tafili, 2025; Tafili et al., 2024a). Ignoring this anisotropy can lead to significant inaccuracies, particularly in cases involving complex stress states or large deformations (Tafili and Triantafyllidis, 2019).

To address this, more advanced constitutive models have been developed that specifically incorporate inherent anisotropy, e.g. Dafalias et al. (2006), Liu et al. (2013), Dejaloud and Rezania (2021), He et al. (2023), Mašín and Rott (2014), Mašín (2014), Tafili and Triantafyllidis (2020b), Tafili et al. (2022a). These models allow for a more realistic prediction of clay behaviour, especially in problems where directional effects play a critical role, such as slope stability, excavation-induced deformations, and the response of offshore foundations. A summary of various constitutive model approaches is presented in Fig. 1. Continued refinement of these models, supported by experimental validation and

* Corresponding author.
E-mail address: duy.anh.dao@tuhh.de (D.A. Dao).

https://doi.org/10.1016/j.compgeo.2025.107537
Received 13 May 2025; Received in revised form 4 July 2025; Accepted 29 July 2025
Available online 18 August 2025

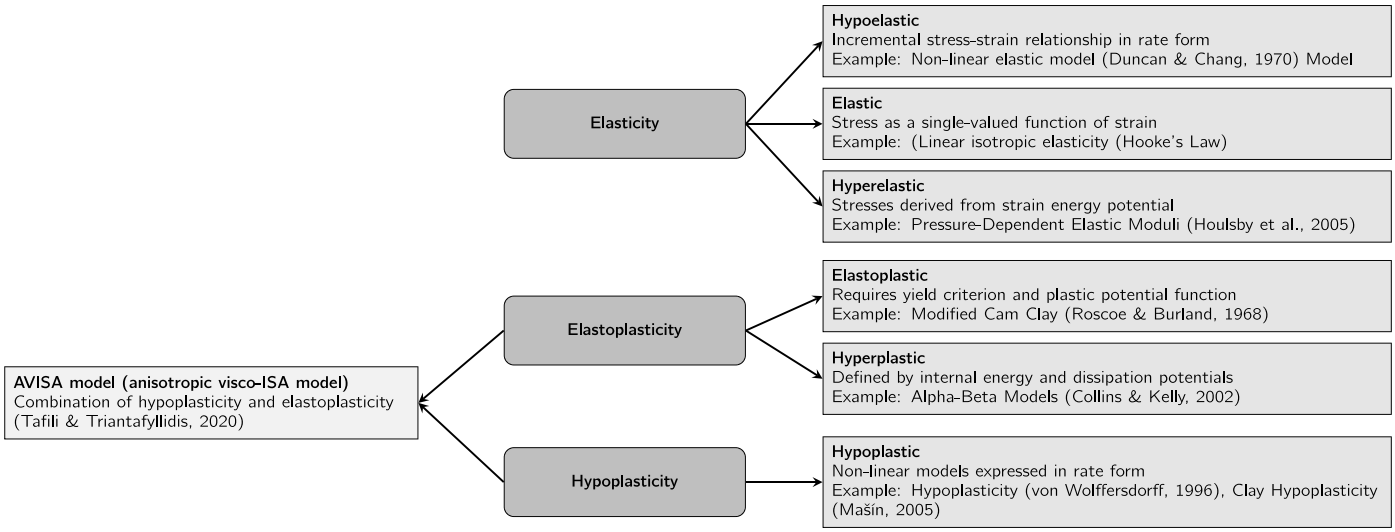

Fig. 1. Classification of constitutive models including AVISA for continuum analysis of geomaterials, according to Carter (2024).

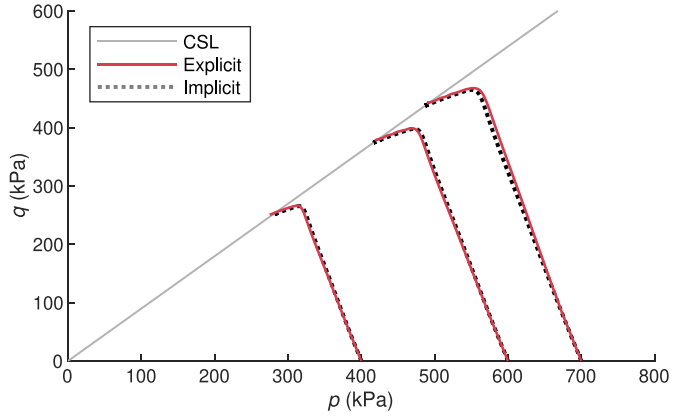

Fig. 2. Comparison of triaxial element test *p-q* results using the implicit and explicit formulations of AVISA for Frankfurt clay.

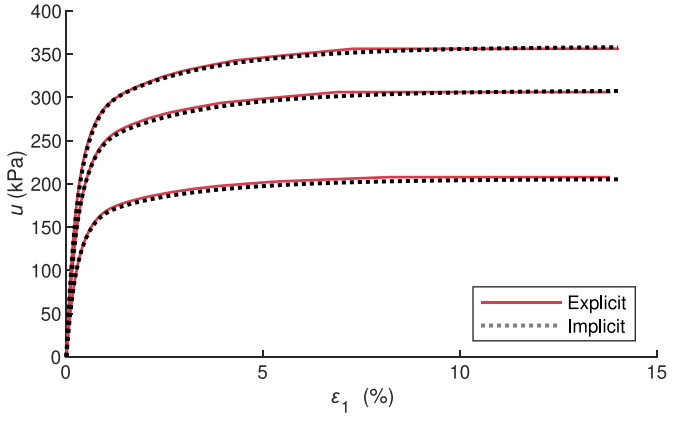

Fig. 3. Comparison of triaxial element test pore pressure results using the implicit and explicit formulations of AVISA for Frankfurt clay.

numerical implementation, remains a key area of research in geotechnical engineering. The Anisotropic Visco-Intergranular Strain Anisotropy (AVISA) model (Tafili and Triantafyllidis, 2020a) incorporates inherent anisotropy through the introduction of a transversal hypoelastic stiffness tensor. The AVISA model has been applied in various studies for advanced numerical simulations and reliable prediction of soil behaviour (Duque et al., 2022). Applications include the back-analysis of piled raft performance (Tafili et al., 2023b), evaluation of lateral loading on monopile foundations, and back-calculation of centrifuge test results (Tafili and Triantafyllidis, 2020a; Tafili et al., 2024c). Furthermore, the model has been coupled with the High-Cycle Accumulation model (Staubach et al., 2022) to predict lateral displacements over thousands of loading cycles. These applications highlight the capability of the AVISA model to simulate a wide range of soil responses, from monotonic to cyclic loading and from rate-dependent to rate-independent material behaviour of cohesive soils, while consistently accounting for both inherent and induced anisotropy.

Although some existing constitutive models incorporate these influences at small strain levels, large deformation finite element (LDFE) analyses often rely on a simplified assumption of isotropic soil stiffness. While there are LDFE modelling applications that focus on fine-grained soil modelling (Li et al., 2023; Dao et al., 2023; Staubach et al., 2023; Wiesenthal and Henke, 2024; Wang and Bienen, 2016; Hossain et al., 2015), the consideration of OCR and anisotropy is either indirect or not addressed. While both the AVISA model and explicit time integration schemes with Lagrangian FEM and the CEL approach are established individually, their combination has not been explored previously. Due to convergence challenges typically associated with advanced soil models, such integration for large deformation analysis is technically difficult. This work presents the first successful implementation of a hypoplastic model for fine-grained soils that incorporates stiffness anisotropy, overconsolidation influence, rate dependency, and critical state behaviour in explicit numerical methods, including dynamic and Coupled Eulerian–Lagrangian (CEL) analyses involving large deformations. In the absence of relevant experimental data, the aim of this study is to verify whether the model can reproduce key mechanical trends under realistic soil conditions involving large deformations, rather than to replicate specific field measurements.

2. Anisotropic visco-intergranular strain anisotropy (AVISA) model

The AVISA model by Tafili and Triantafyllidis (2020a) presents a visco-hypoplastic model coupled with the Anisotropic Intergranular Strain Anisotropy (ISA). ISA was originally introduced by Fuentes and Triantafyllidis (2015) for sand and further coupled with various constitutive models to improve their abilities upon cyclic loading (Fuentes

et al., 2018, 2021; Tafili et al., 2022b; Medicus et al., 2023; Lascarro et al., 2024) as well as modified to meet the specific requirements of fine-grained soils in Tafili and Triantafyllidis (2020a).

2.1. Model formulation

The mechanical model formulation adopts the hypoplastic framework, incorporating the total strain rate $\dot{\boldsymbol{\varepsilon}}$, hypoplastic strain rate $\dot{\boldsymbol{\varepsilon}}^{\mathrm{hp}}$, and viscous (time-dependent) strain rate $\dot{\boldsymbol{\varepsilon}}^{\mathrm{vis}}$. The stress rate tensor $\dot{\boldsymbol{\sigma}}$ is expressed as:

$$\dot{\boldsymbol{\sigma}} = m\,\mathsf{E} : \left(\dot{\boldsymbol{\varepsilon}} - y_{\mathrm{h}}\dot{\boldsymbol{\varepsilon}}^{\mathrm{hp}} - \dot{\boldsymbol{\varepsilon}}^{\mathrm{vis}}\right) \tag{1}$$

with a transversal hypoelastic stiffness tensor as a function of stress and void ratio, $\mathsf{E} = f(\boldsymbol{\sigma}, e)$. The transversal isotropic elastic stiffness is approximated following Graham and Houlsby (1983), with the Young's modulus in vertical direction $E = E_{\mathrm{v}}$, the shear modulus in vertical direction G_{v}, the Poisson's ratio in horizontal direction $\nu = \nu_{\mathrm{h}}$ and the scalar parameter α as the anisotropy coefficient. The latter one governs the relationship between the horizontal and the vertical stiffness components as follows:

$$\frac{G_{\mathrm{h}}}{G_{\mathrm{v}}} = \left(\frac{E_{\mathrm{h}}}{E_{\mathrm{v}}}\right)^{\frac{1}{2}} = \frac{\upsilon_{\mathrm{h}}}{\upsilon_{\mathrm{vh}}} = \alpha \tag{2}$$

This relation reflects the assumption that shear stiffness scales with the geometric mean of the directional Young's moduli, as shear deformation involves both vertical and horizontal directions.

In Eq. (1), m and y_{h} are scalar functions that consider the influence of intergranular strain by increasing the elastic stiffness tensor and decreasing the hypoplastic strain rate, $\dot{\boldsymbol{\varepsilon}}^{\mathrm{hp}}$, upon cyclic loading. The evolution equation of the hypoplastic strain rate, $\dot{\boldsymbol{\varepsilon}}^{\mathrm{hp}}$, is as follows:

$$\dot{\boldsymbol{\varepsilon}}^{\mathrm{hp}} = Y\|\dot{\boldsymbol{\varepsilon}}\|\,\mathbf{m} \tag{3}$$

The degree of nonlinearity, denoted as Y, is a function of both the stress state and the void ratio, expressed as $Y = f(e, \boldsymbol{\sigma})$. In contrast, the flow rule, represented by $\mathbf{m}$, depends solely on the stress state and is given by $\mathbf{m} = f(\boldsymbol{\sigma})$. Hereby, the following three additional parameters are introduced: the reference void ratio, e_{i0}, the slope of the critical state line in the deviatoric stress vs. mean effective stress plane $(p' - q)$ in triaxial compression, M_{c}, and the constant defining the initial slope of the loading surface, f_{b0}.

The viscous strain rate, $\dot{\boldsymbol{\varepsilon}}^{\mathrm{vis}}$, employs the viscosity index, I_{v}, as a model parameter, without introducing a singularity in the model when I_{v} approaches zero, as follows:

$$\dot{\boldsymbol{\varepsilon}}^{\mathrm{vis}} = I_{\mathrm{v}}\,\lambda\frac{1}{t_0}\left(\frac{1}{\mathrm{OCR}}\right)^{1/I_{\mathrm{v}}}\mathbf{m} \tag{4}$$

The introduction of the multiplier $I_{\mathrm{v}}\,\lambda$ ensures the suitability of the model for both viscous (rate-dependant, $I_{\mathrm{v}} \neq 0$) and non-viscous (rate-independant, $I_{\mathrm{v}} = 0$) fine-grained soils. For $I_{\mathrm{v}} = 0$, the product $I_{\mathrm{v}} \cdot \lambda$ vanishes, and the viscous term in Eq. (4) is defined to be zero, allowing the model to reproduce purely rate-independent plastic behaviour and reach the critical state through the hypoplastic strain rate formulation, see Eq. (3). λ is the compression index of fine-grained soils to be calibrated based on the normal compression line. The overconsolidation ratio OCR accounts for the stress tensor as well as the void ratio. The reference time t_0 can be set to 1 sec, depending on the time units used for calibrating I_{v} and those applied in the current simulation.

To improve the performance of hypoplastic models under cyclic and small strain loading conditions, the intergranular strain (IGS) concept was introduced by Niemunis and Herle (1997). The elastoplastic reformulation, ISA, defines a yield and bounding surface in the IGS space, which govern the onset and full mobilisation of intergranular strains. These mechanisms enable a smooth transition from reversible to irreversible behaviour and capture stiffness degradation, ratcheting, and strain accumulation effects under cyclic loading. A summary of all model parameters and initial state variables is provided in Section 2.2.

The original AVISA model, like most advanced soil models, has been formulated in small to medium strain kinematics. In this study, it is embedded within a numerical framework (CEL and explicit Lagrangian FEM) that accounts for large displacements and rotations. This allows for the simulation of large deformation boundary value problems, while the constitutive response is evaluated in the co-rotational reference frame under the small to medium strain assumption.

2.2. Constitutive model parameters

The current version of the AVISA model includes 15 parameters, listed in Table 1. These parameters are grouped according to their function within the constitutive formulation:

- parameters defining the transversely isotropic hypoelastic stiffness,
- parameters controlling small strain stiffness and the influence of intergranular strain,
- parameters related to the critical state and bounding surfaces, and
- viscosity-related parameters.

A detailed summary of the parameter determination and an approximate range of them as well as details on the initialisation of the state variables are presented in Tafili and Triantafyllidis (2020a), Tafili et al. (2023b). In summary, the AVISA model requires the initialisation of the void ratio and the intergranular as well as back-intergranular strain tensor. In all subsequent simulations, the intergranular strain tensor is initialised in a fully mobilised state in the isotropic direction as $\mathbf{h} = R/\sqrt{3}\mathbf{1}$, while the back intergranular strain tensor is set to $\mathbf{c} = \mathbf{h}/2$.

The soil in the following simulations is modelled as Frankfurt clay, with material properties listed in Table 2 and model parameters calibrated by Tafili et al. (2023b), as presented in Table 1.

2.3. Implementation of the AVISA model in explicit analyses

Previous applications of the AVISA model, originally programmed as user material subroutine (UMAT), were limited to small to moderate strain FE analyses using an implicit solution scheme in Abaqus/Standard (Tafili et al., 2024c,b), numgeo (Tafili et al., 2024c), Tochnog (Tafili et al., 2023b) and Plaxis (Rafai et al., 2025).

However, processes such as anchor dragging (Dao and Grabe, 2022; Dao and Dicke, 2022), suction pile penetration (Stapelfeldt et al., 2020), or pile penetration (Dao et al., 2024, 2025; Tafili et al., 2025) involve large deformations, which are better addressed using an explicit integration scheme in Abaqus/Explicit. When performing large deformation analyses, Vectorised User Material subroutines (VUMAT), which differ from a UMAT, are required.

Unlike a UMAT, which updates data incrementally at each integration point and requires the material Jacobian matrix, a VUMAT processes all integration points in a batch and does not need the Jacobian. It also handles stress and strain storage differently, using for three-dimensional elements the stress component order $(\sigma_{11}, \sigma_{22}, \sigma_{33}, \sigma_{12}, \sigma_{23}, \sigma_{13})$ rather than the UMAT convention $(\sigma_{11}, \sigma_{22}, \sigma_{33}, \sigma_{12}, \sigma_{13}, \sigma_{23})$ and tensorial shear strain components $(\varepsilon_{12} = 0.5\,\gamma_{12})$ rather than engineering shear strains (in UMAT: $\gamma_{12} = 2\,\varepsilon_{12}$) (Dassault Systèmes, 2025b,a).

To adapt AVISA for dynamic, large deformation scenarios in ABAQUS/Explicit, the original AVISA implementation was extended by integrating the VUMAT interface developed by Bienen et al. (2014). In contrast to UMAT (used in ABAQUS/Standard), VUMAT requires several specific modifications: as mentioned shear strains must be provided in engineering form (e.g., $\gamma_{12} = 2\varepsilon_{12}$), stress updates must follow an explicit time integration scheme, and internal variables must be explicitly managed. These aspects were incorporated into the AVISA code. The adopted interface handles the transformation between tensorial and engineering shear components, assigns all necessary history variables, and restructures the stress update to match VUMAT

Table 1
AVISA parameters of Frankfurt clay by Tafili et al. (2023b).

Parameter	Symbol	Frankfurt clay	Determination method
Transversal (hypo)elasticity:			
Compression index	λ	0.116	Triaxial, oedometer test
Swelling index	κ	0.031	Oedometer test
Poisson's ratio	ν_h	0.23	Trixial test (different cutting directions)
Anisotropic coefficient	α	1.5	Triaxial test (different cutting directions)
Critical and loading surface:			
Critical state slope	M_c	0.898	Undrained triaxial test
Max. void ratio at $p_{ref} = 1$ kPa	e_{i0}	1.48	Oedometer test
Loading surface factor	f_{b0}	1.4	Triaxial test on overconsolidated sample
Viscosity:			
Viscosity index	I_v	0.030	Oedometer test (different deformation rates)
Viscosity exponent	n_{OCR}	0.4	Oedometer/triaxial test (different deformation rates)
Intergranular strain anisotropy (ISA):			
Stiffness factor	m_R	2.5	Resonant column test/Calibration
ISA yield surface radius	R	1.8×10^{-4}	Resonant column test/Calibration
ISA hardening parameter	β_0	0.1	Cyclic triaxial test
Min. ISA exponent	χ_0	5	Cyclic triaxial test
Max. ISA exponent	χ_{max}	60	Cyclic triaxial test
Accumulation rate factor	C_a	0.001	Cyclic triaxial test

Table 2
Characteristics of Frankfurt clay.

Parameter	Value	Unit	Description
w_L	0.75	–	liquid limit
w_P	0.28	–	plastic limit
γ_s	13.5	kN/m^3	dry unit weight
γ	18.5	kN/m^3	unit weight

Table 3
Parameters of the upper soil layers (Moormann et al., 2018).

Soil type	γ (kN/m^3)	φ (°)	E_s (MN/m^2)
Sub-base material	20.4	42.5	180
Rhine sand	18.6	32.5	75
Fine sand	17.7	32.5	70

conventions. These additions extend the original AVISA framework and ensure compatibility with explicit dynamic simulations. The robustness of the interface has been validated in multiple benchmark studies by Bienen et al. (2014), and it enables consistent material behaviour across both UMAT and VUMAT implementations. Particular implementation challenges include numerical stability at large deformations, proper stress update in the Eulerian mesh, and consistent handling of internal variables. The successful use of AVISA in this context demonstrates the model applicability beyond small strain problems and opens new opportunities for realistic large strain geotechnical simulations.

Figs. 2 and 3 present a representative triaxial test, evaluated as an element test using the constitutive model applied in the subsequent simulations. The model was implemented both in Abaqus/Standard, via the previously developed implicit routine, and in Abaqus/Explicit, using the newly implemented routine designed for dynamic and LDFE analyses. To quantify the agreement between the two implementations, a root mean square error (RMSE) was calculated and normalised by the mean of the corresponding curves. With an nRMSE of 1 %, the comparison confirms excellent consistency, demonstrating that the new explicit routine reliably reproduces the simulations conducted with Abaqus/Standard in this study, as well as with Tochnog and the Incremental Driver, available open access at: Tafili (2024), reported in Tafili et al. (2023b).

3. Numerical methods

In continuum mechanics, motion can be described using different formulations, which influence how FE methods are applied in geotechnical simulations. The Lagrangian formulation represents motion as a function of material coordinates and time, while the Eulerian formulation expresses it in terms of spatial coordinates and time. The choice of formulation is particularly relevant for simulations involving large deformations and dynamic processes.

3.1. Lagrangian formulation

In the Lagrangian approach, each node of a FE mesh moves together with the material as it deforms. This allows for precise tracking of material surfaces. However, as the material deforms, the mesh deforms as well, which can lead to element distortion and numerical difficulties. Because each element remains associated with the same material, there is no mixing of different materials within an element. The Lagrangian formulation is the basis of the classical FEM.

3.2. Eulerian formulation

The Eulerian approach, in contrast, keeps the spatial mesh fixed while materials move through it. This formulation is suitable for large deformations since the mesh does not change shape. However, this means that elements may contain multiple materials or even be empty, leading to numerical diffusion effects. Additionally, precise surface tracking is not possible in a purely Eulerian formulation. The Eulerian Volume Fraction (EVF) is used here, which indicates the percentage by which an element of the FE mesh is filled with material. Consequently, the elements are not necessarily completely filled with material. Fig. 4 shows both formulations in comparison.

3.3. Coupled Eulerian-Lagrangian (CEL) method

The CEL method combines both formulations, see Fig. 5, making it well-suited for problems involving large deformations and interactions between moving materials and structures (Noh, 1963). In CEL simulations, Lagrangian elements move freely through an Eulerian mesh until contact occurs, at which point the Eulerian–Lagrangian contact formulation governs their interaction. Unlike traditional contact methods, this approach does not require predefined contact conditions; instead, contact is detected as the simulation progresses.

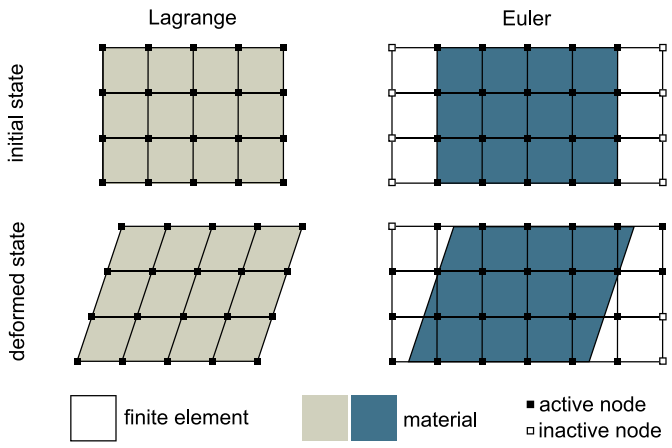

Fig. 4. Lagrangian and Eulerian formulation.

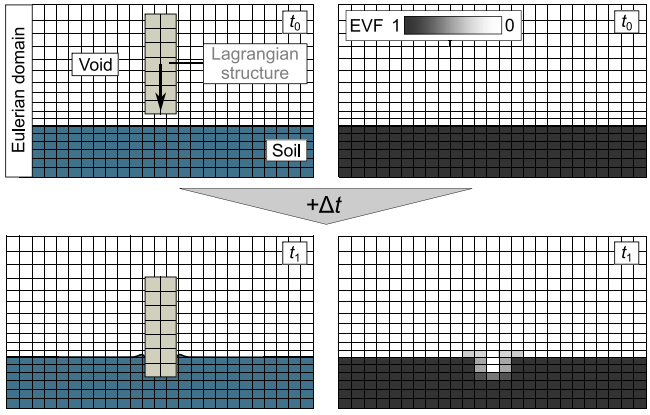

Fig. 5. 2D example of a pile penetration process applying CEL.

CEL simulations involve two phases. During the Lagrangian phase, material motion is tracked by associating Eulerian nodes with the material and updating mesh deformation at each time step. In the transport phase, material flow through the mesh is remapped to handle large deformations while preserving force accuracy. A sufficiently small time step is required to avoid mesh distortion.

The CEL method integrates both Lagrangian and Eulerian elements, as presented by Noh (1963) and Benson (1992), considering the contact between them. While the pile is represented using Lagrangian elements, the strongly deforming soil is modelled using Eulerian elements. The effectiveness and reliability of this approach in geotechnical engineering is demonstrated in the works by Grabe and Dao (2024), Dao et al. (2023) and Bienen et al. (2021), among others. The numerical analyses are based on the commercial software package Abaqus, within which the CEL method is implemented using an explicit central difference time integration method, see Dassault Systèmes (2016).

3.4. Explicit time integration

The CEL method requires a numerical scheme suitable for dynamic problems, particularly when dealing with large deformations. Explicit time integration is commonly used in such cases because it allows for efficient handling of contact interactions and material flow. This method calculates the solution step-by-step using values from previous time increments, avoiding the need for iterative solvers (Bathe, 2006). However, explicit time integration is computationally expensive due to the requirement for small time steps to ensure numerical stability, especially in three-dimensional simulations. By integrating explicit time integration with the CEL method, it becomes possible to simulate dynamic processes and large deformation problems in geotechnical engineering.

4. Stability of a crane under dynamic turning

Construction machinery is inherently prone to overturning due to its high centre of gravity. Overturning incidents regularly lead to economic losses amounting to millions of dollars and result in injuries or fatalities, in some cases affecting more than one hundred people per accident (Kargar et al., 2022; Ross et al., 2007). A critical factor contributing to overturning is the failure of the ground beneath the crawler tracks. Existing standards that define the permissible operational conditions of construction machinery on working platforms rely on simplified models that calculate stress distribution using purely static analyses, assuming a rigid and stable platform (Construction Plant-hire Association, 2014; BS EN 16228-1, 2021).

The European standard BS EN 16228-1 (2021) defines the stability of construction machinery as the ratio between the bearable load and actual load, ensuring that the equipment neither oversinks nor tips over. This standard assumes a trapezoidal or triangular stress distribution beneath the crawler tracks, depending on the loading conditions, while neglecting potential subsoil failure. This simplification, known as the stress trapezoid method, reduces all forces acting on the machine to a resultant point load. Williams Riquer et al. (2022) extended these assumptions by incorporating potential soil failure mechanisms into a multibody dynamical model. Furthermore, field tests by Moormann et al. (2018) and Keller and Arvidsson (2016) demonstrated nonlinear stress distributions beneath machinery tracks. Insufficient subsoil-bearing capacity is a critical factor that can significantly impair a machine's stability (Urbański and Richter, 2021). Due to poor ground conditions or a shift in the centre of mass into a critical range, accidents tend to occur (Edwards and Holt, 2010). Possible ground failure mechanisms include general shear failure, slope failure, and excessive settlements, which can induce tilting and compromise the machine's stability. Nonlinear soil behaviour and structure–soil-interaction are critical for assessing the safety of construction machinery operating on soft soils. In this study, these effects are captured by applying the AVISA model within an explicit dynamic simulation, using a purely Lagrangian motion formulation to represent the uppercarriage rotation of a crane in Abaqus/Explicit. The numerical analysis is focused on computing the ground pressure distribution beneath the crawler tracks as well as the tilting and rolling behaviour of the construction machine under varying overconsolidation ratios OCR.

4.1. Existing field tests

The calculated ground pressure distribution is compared to field tests conducted by Moormann et al. (2018). The tests were performed at a LIEBHERR-owned test site using the telescopic crawler crane LTR 1220, shown in Fig. 6. The LTR 1220 has a maximum lifting capacity of 220 t, with a self-weight of 92.5 t without ballast and 182.5 t with counterweights. The crawler tracks measure 9.13 m in length and 1.0 m in width. Prior to testing, an initial excavation of 0.5 m depth was carried out over an area of 3.0 m × 14.0 m to install earth pressure cells, see Fig. 7.

4.2. FE model of the crane

The construction machine model was created as a dynamic multibody model to simulate movements and interactions of the interconnected, geometrically simplified, ideally rigid bodies. The inclination of the crane arm was estimated at 25 ° and kept constant throughout the

Table 4
Data of jacked open-ended tubular piles in fine-grained soils.

Source	Pile outer diameter D (m)	Pile wall thickness t (m)	Clay consistency	Data type
Wang et al. (2021)	0.40	0.095	Plastic	Field tests
Wang et al. (2022), Song et al. (2022)	0.14	0.030	Soft	Laboratory tests
Wiesenthal and Henke (2024)	0.50	0.040	Stiff	Simulation
Bai et al. (2024)	0.60	0.110	Soft	Simulation

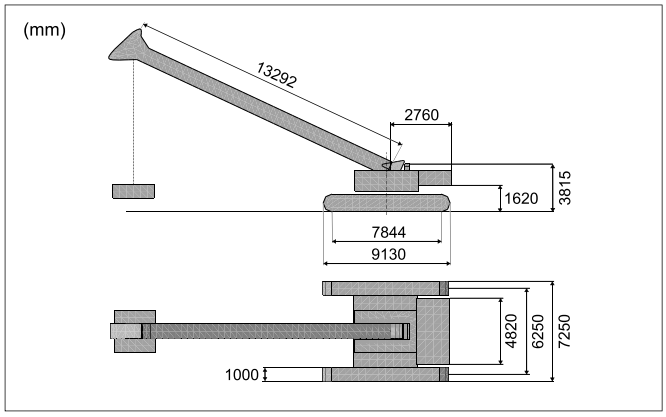

Fig. 6. Geometries of crane model.

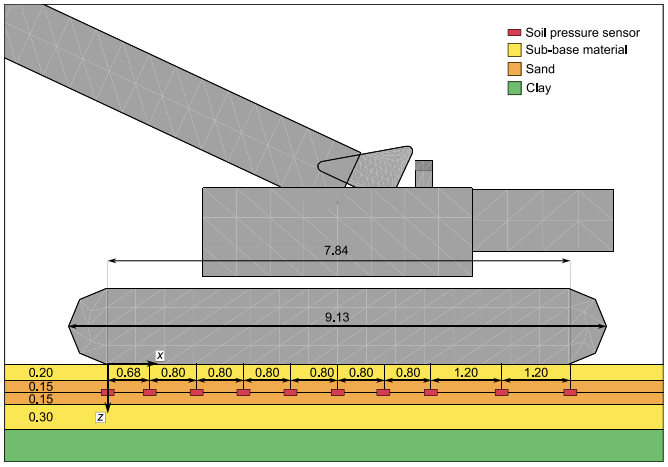

Fig. 7. Position of sensors with measurements in m (Moormann et al., 2018).

simulation. The hook load consists of a cuboidal block with a weight of 32 t, suspended 1 m above the ground and coupled by a link connector to the crane arm. The soil friction coefficient was estimated at 0.667, based on the interaction between the track plate material (polyamide) and the underlying gravel. Fig. 8 shows the discretised soil domain with its boundary conditions. It consists of cuboidal elements of type C3D8R with an edge length of approximately 0.1 m. A finer mesh was created directly under the crane to ensure a higher accuracy of the subsoil reactions. A coarser mesh resolution was used as less soil reaction is expected in the outer area. The outer element edge lengths were set to 1 m. The soil model length and width are six times the outer dimensions of the crane to prevent wave reflections at the model boundaries. The soil model consists of five successive layers. The simulation used Mohr–Coulomb plasticity for the coarse-grained soil layers with constitutive parameters listed in Table 3 and AVISA for the clay layer modelled as Frankfurt clay.

The simulations were conducted in three distinct steps. In the first step, the boundary conditions for all model components are applied, including the initialisation of the in-situ K_0 stress state in the soil. The motion of the lateral boundaries and the bottom surface is restricted in the normal direction throughout the entire simulation. The second step involves the initialisation of gravity, see Fig. 9. In the third step, the rotation of the uppercarriage is initiated with a slewing angle of $\phi = 45\,°$. The rotation occurs over 7.5 s, corresponding to a rotation speed of one revolution per minute. In total, the model consists of 673,640 elements and required 122.78 h of computation time using 12 cores to simulate a full 45 ° rotation.

4.3. Results and discussion

Figs. 10 and 11 present the side and front view of the crane model and the computed stress distribution as well as the vertical displacement fields from the FE simulations during tilting and rolling of the crane, respectively. To assess the validity of the numerical approach, Fig. 12 compares the calculated stress distribution beneath the crawler tracks with field measurements reported by Moormann et al. (2018) as well as with analytical estimates following BS EN 16228-1 (2021). The good agreement between the numerical results and field measurements highlights the plausibility and robustness of the simulation approach.

Fig. 13 illustrates the tilting and rolling of the crane at the onset of uppercarriage slewing. The tilt ψ_1 was determined based on the vertical displacements measured at point A (denoted as $u_{z,A}$) and B (denoted as $u_{z,B}$), using the following relationship:

$$\psi_1 = \arctan\left(\frac{|u_{z,A} - u_{z,B}|}{L_1}\right) \tag{5}$$

and the roll ψ_2 was calculated with the vertical displacements at point A and C (denoted as $u_{z,A}$) with

$$\psi_2 = \arctan\left(\frac{|u_{z,C} - u_{z,A}|}{L_2}\right) \tag{6}$$

with $L_1 = 7.844\,\text{m}$ and $L_2 = 7.250\,\text{m}$. The crane continuously tilts forward, causing the rear section of the crawler track to lose ground contact. After reaching its maximum, the forward tilt angle ψ_1 gradually decreases as the slewing angle increases. In contrast, the crane rolls steadily to the side, resulting in a continuous increase of the roll angle ψ_2 (see Fig. 10 right), until it reaches its maximum at the end of the uppercarriage rotation process.

In a further study, AVISA was used to determine the critical overconsolidation ratio (OCR) of the subsoil beneath a construction machine required to allow a $\phi_{\text{complete}} = 45\,°$ rotation of the uppercarriage ($\phi_{\max} \geq \phi_{\text{complete}}$). In a series of simulations, the OCR of the fine-grained layer was systematically varied, see Fig. 14. An OCR of 1 corresponds to normally consolidated (relatively soft) soil, while higher OCR values (> 1) represent overconsolidated, stiffer conditions. When rotating the uppercarriage by ϕ, OCR values of 2, 4, and 6 did not prevent excessive tilting of the tower crane, indicating insufficient stability. Nonetheless, overall system stability increases sharply with OCR. The tested OCR values of 8, 10, and 12 provided sufficient stability for a full uppercarriage rotation of 45 °. Based on the results, the minimum required OCR is estimated to lie between 6 and 8. The exponential fit, see Eq. (7), supports this assumption and indicates that an OCR of 6.302 is sufficient to ensure stability for the specified $\phi_{\text{complete}} = 45\,°$ rotation.

$$\phi_{\max} = 0.31\, e^{0.79\,\text{OCR}}, \tag{7}$$

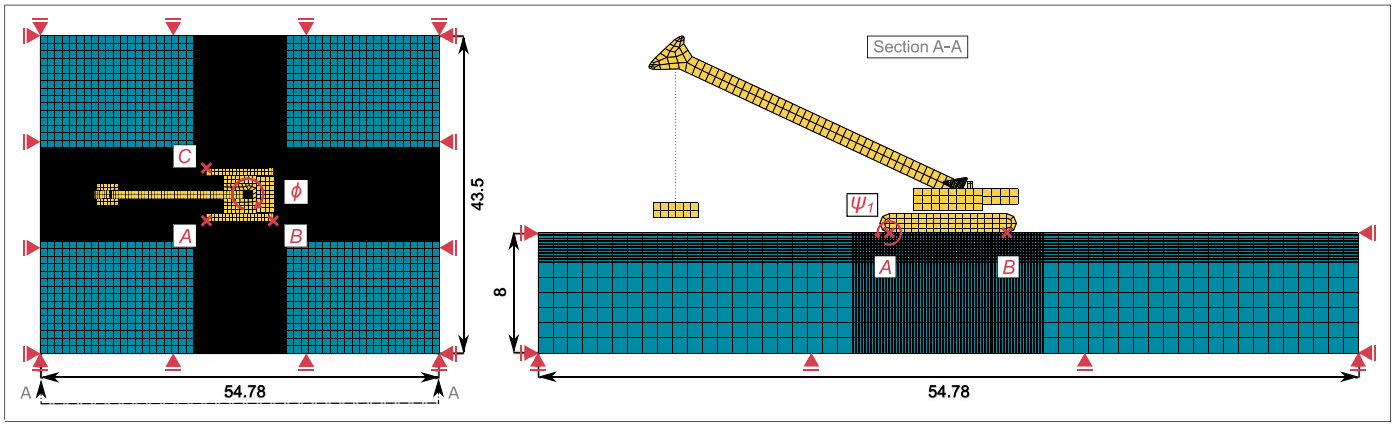

Fig. 8. Crane model assembly.

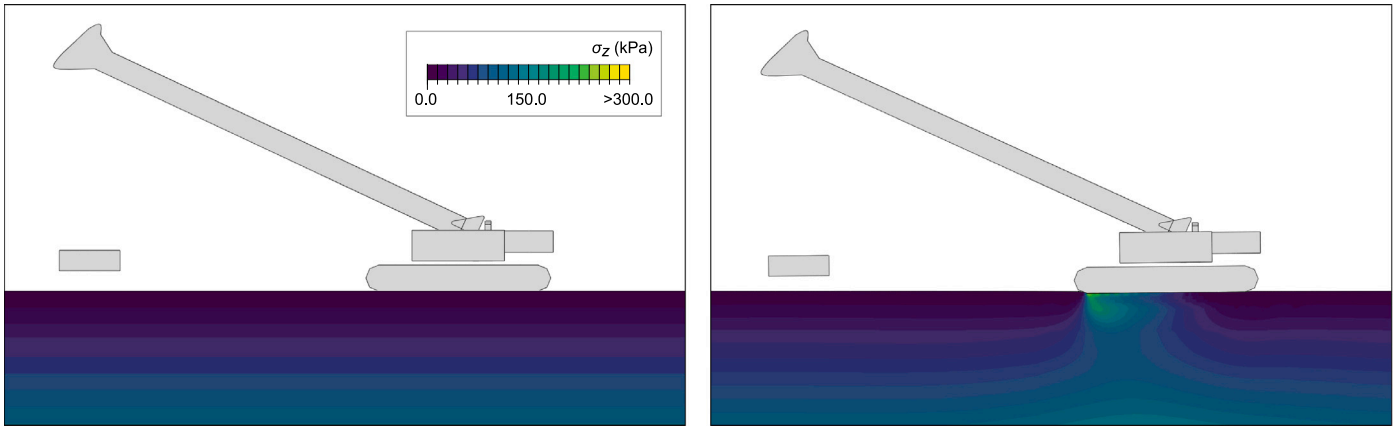

Fig. 9. Initial stress state before and after gravity initialisation.

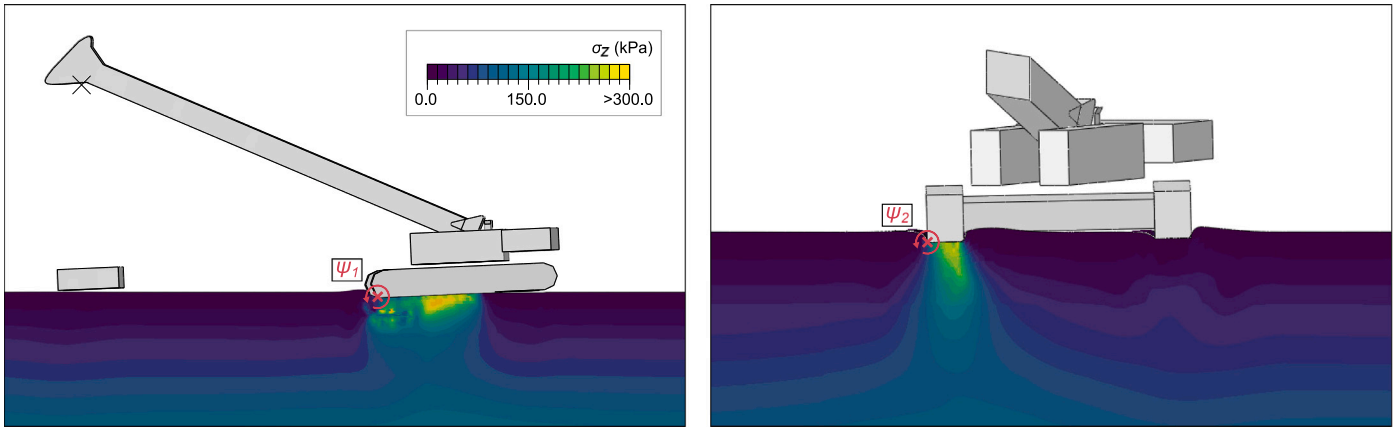

Fig. 10. Side view of crane model during tilting and front view during rolling of the crane and vertical stress distribution beneath the tracks.

The simulations demonstrate that the consideration of nonlinear soil properties and structure–soil-interaction effects is crucial for accurate modelling of construction machinery on soft soils. Moreover, The simplified parametric study illustrates how ground improvement measures, such as compaction or surcharge loading to increase the OCR, may enhance crane stability in practice.

5. Pile penetration

This section presents explicit LDFE analyses of pile penetration in overconsolidated, anisotropic fine-grained soil using the CEL method in Abaqus/Explicit. Large soil deformations during pile installation and direction-dependent strength characteristics need a CEL-based

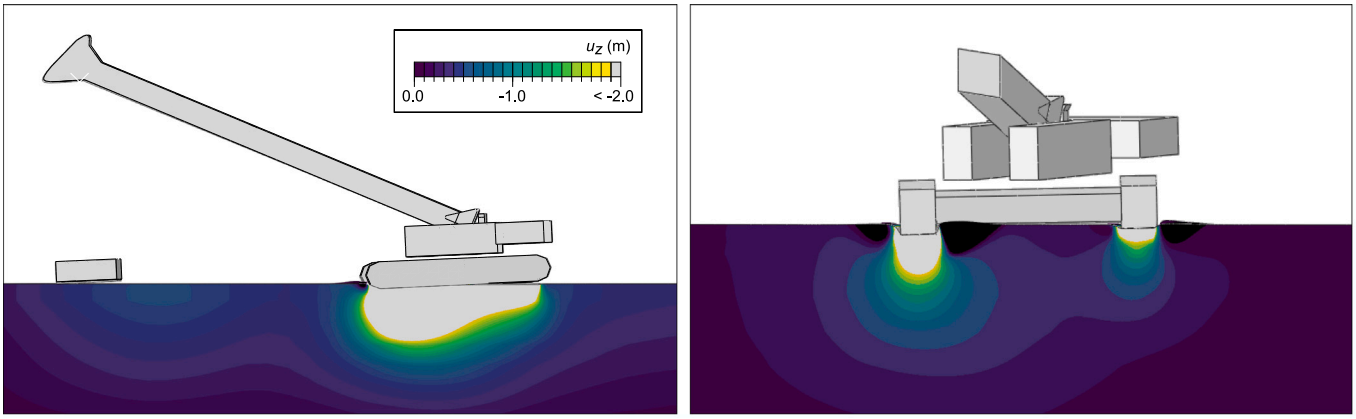

Fig. 11. Side and front view of the displacement field beneath the track of the crane during rolling.

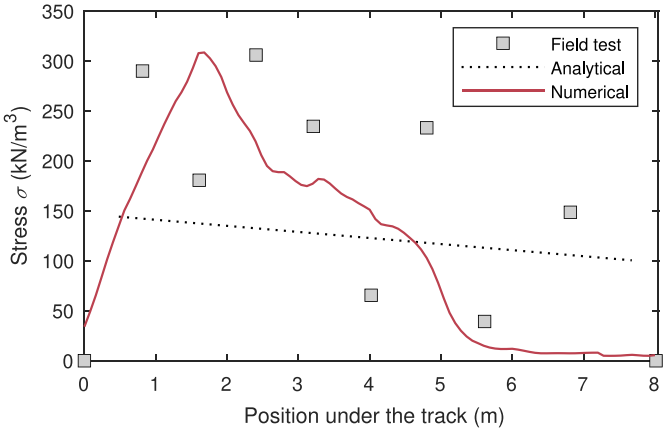

Fig. 12. Comparison to field tests.

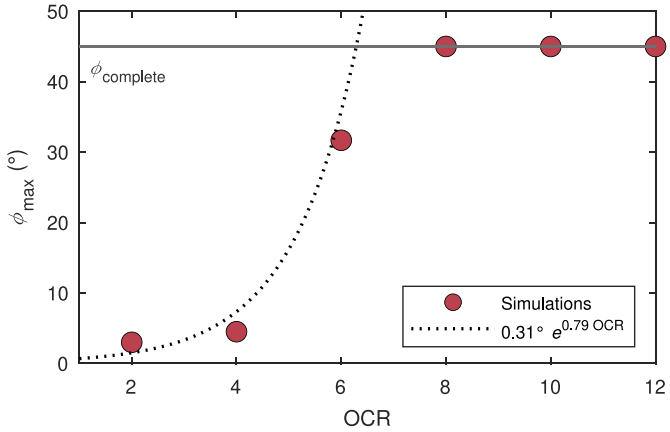

Fig. 14. Crane stability dependent on OCR.

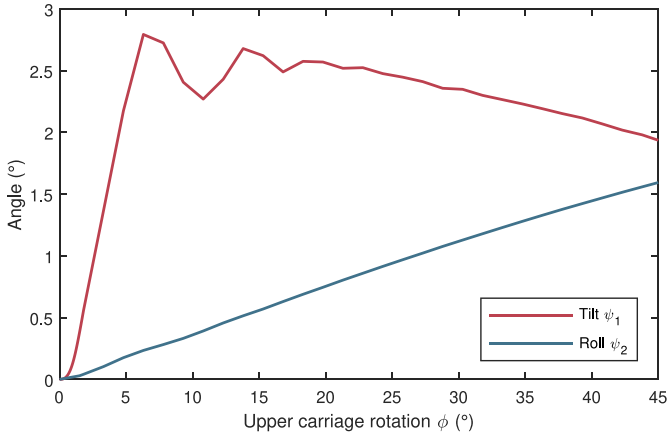

Fig. 13. Tilt and roll during uppercarriage rotation.

anisotropic constitutive framework under overconsolidated conditions which is accounted for by AVISA. The following simulations model the vertical penetration of a pile into the soil. The numerical model aims to capture the essential structure–soil-interaction mechanisms.

5.1. CEL model

Fig. 15 presents the 3D CEL model which includes one quarter of the rigid pile and the soil body. The pile is positioned 0.05 m above the homogenous soil at the beginning of the simulation. To accommodate potential soil heave, an initially empty volume (light grey) above the soil (turquoise) is included. Lagrangian elements discretise the pile and Eulerian elements discretise the soil and void. A refined mesh is applied in the vicinity of the pile to capture the wall thickness realistically, while the element size increases progressively away from the pile to reduce dynamic wave reflections at the boundaries. The surrounding soil is modelled as Frankfurt clay using the AVISA constitutive model with the parameters listed in Table 1 from Tafili et al. (2023b). The interaction between the pile and the soil is represented by a frictional contact formulation following the standard Coulomb model. Here, the friction coefficient is defined as $\tan(1/3\varphi_c)$, where $\varphi_c = \arcsin(3M_c/(6+M_c))$ denotes the critical state friction angle of the soil. This choice was made due to current limitations in the availability of advanced contact models for CEL analyses. Moreover, the interaction was assumed to be dominated by normal contact forces. As the objective of this work is to reproduce general trends observed in the limited available experimental and field data, simplified assumptions were necessary. Nonetheless, the use of more advanced contact models would be appropriate for future studies aiming to capture interface behaviour in greater detail, as proposed by Aguiar et al. (2011), Duriez and Vincens (2015), Fakharian

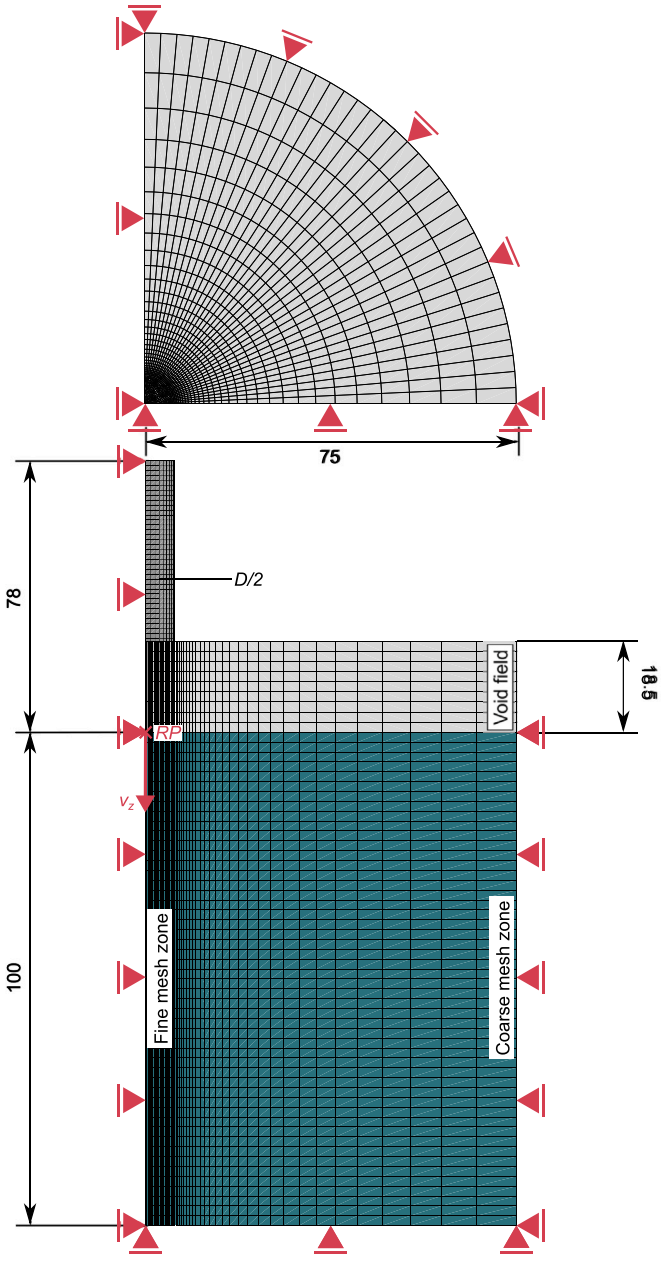

Fig. 15. Top and side view of the model for simulating pile penetration and boundary conditions with lengths given in m.

and Evgin (2000), Hu and Pu (2003), Liu et al. (2014), Arnold and Herle (2006) and Stutz et al. (2017).

The simulation of the penetration process is performed under displacement control in three sequential steps. In the first step, the initial boundary conditions and the earth pressure at rest are established. The second step applies the gravitational forces to the system, with the pile still positioned above the soil. In the third step, the vertical displacement of the pile is initiated by imposing a velocity v_z of 1 m/s at the reference point *RP*, as illustrated in Fig. 15. The selected mesh, consisting of 33,503 elements, was identified as the optimal configuration, providing an effective balance between computational efficiency and mesh independence. With this mesh, the total computation time was 5.72 h using 12 cores.

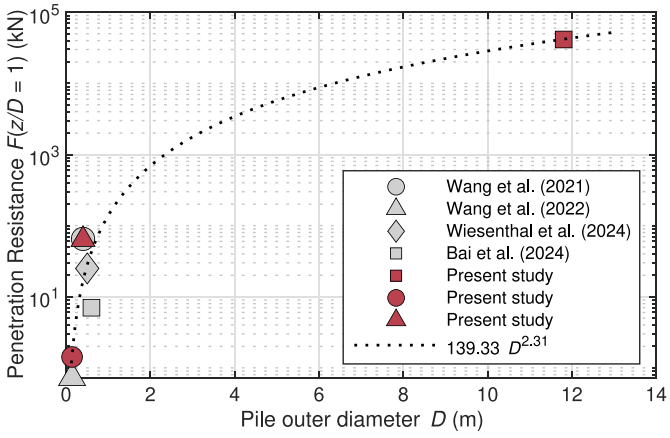

Fig. 16. Penetration resistance over pile outer diamater: comparison of simulations and field data of jacked open-ended tubular piles in fine-grained soils.

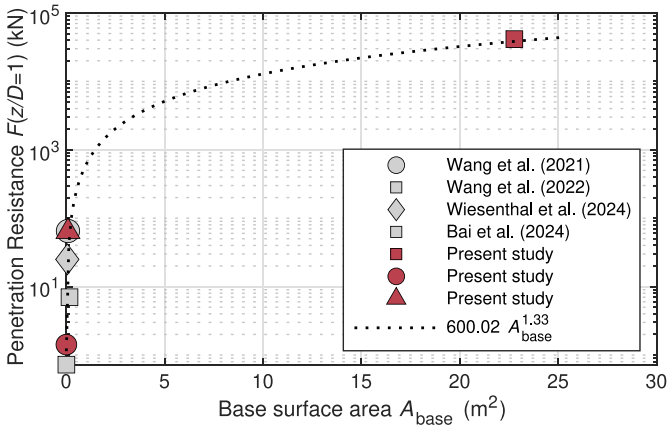

Fig. 17. Penetration resistance over pile base surface area: comparison of simulations and field data of jacked open-ended tubular piles in fine-grained soils.

5.2. Comparison with existing studies

The available data on jacking open-ended tubular piles into fine-grained soils remain limited. Table 4 provides an overview of the few published studies, detailing the pile outer diameter, wall thickness, and soil consistency for each test.

Field and laboratory jacking tests have been reported by Wang et al. (2021, 2022) and Song et al. (2022). Additional field tests were conducted by Doherty et al. (2010), Doherty and Gavin (2011), whose data were later used to validate the approach proposed by Wiesenthal and Henke (2024, 2025); however, it is important to note that penetration forces near the surface were not recorded in their measurements. Instead of employing an FE model, Bai et al. (2024) simulated the pile installation process using the discrete element method (DEM).

All tests involve fine-grained soils. However, the soil stiffness and overconsolidation levels vary substantially across the studies. Despite these differences, comparison of the simulation results of this study with the available data shows that the predicted penetration forces fall within a realistic and plausible range, as illustrated in Figs. 16 and 17.

5.3. Results and discussion

The analysis focuses on the impact of soil anisotropy and overconsolidation on pile behaviour during the penetration process. Anisotropic conditions were controlled by varying the anisotropic coefficient α. Values of $\alpha < 1$ represent conditions where horizontal stiffness is

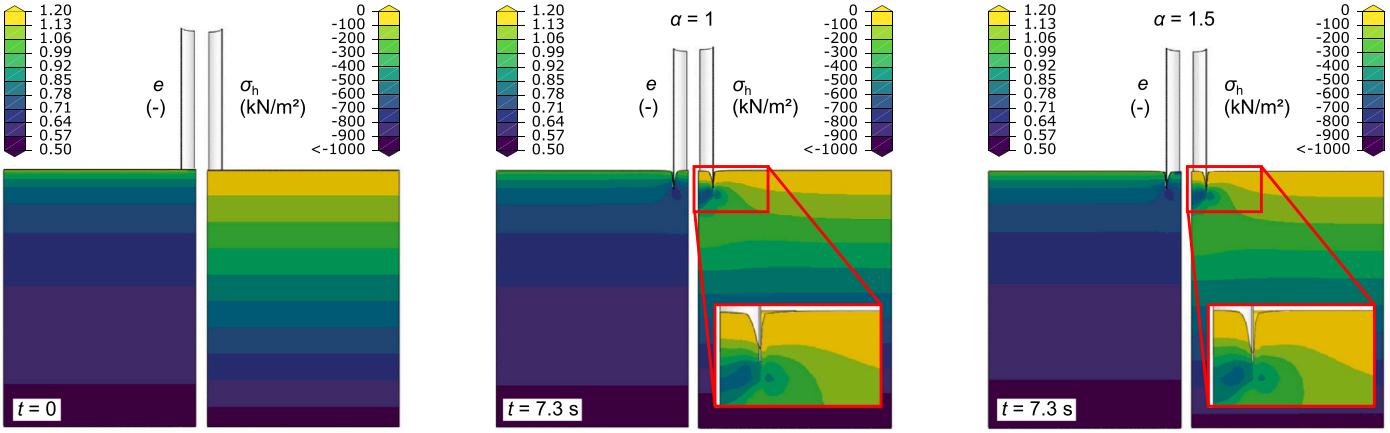

Fig. 18. Void ratio and horizontal stress distribution before and after pile penetration.

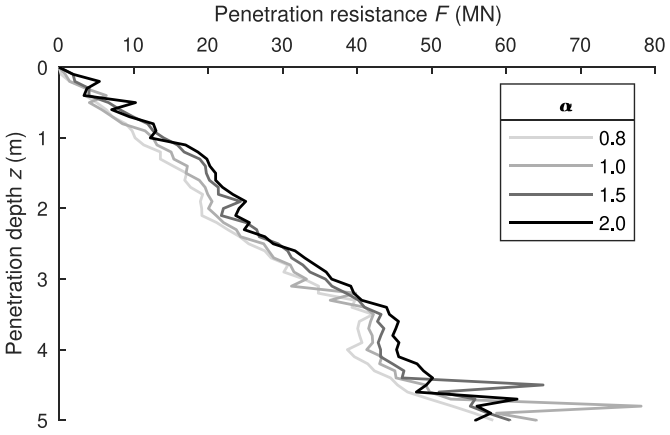

Fig. 19. Penetration resistance as a function of penetration depth for different values of the anisotropy coefficient α.

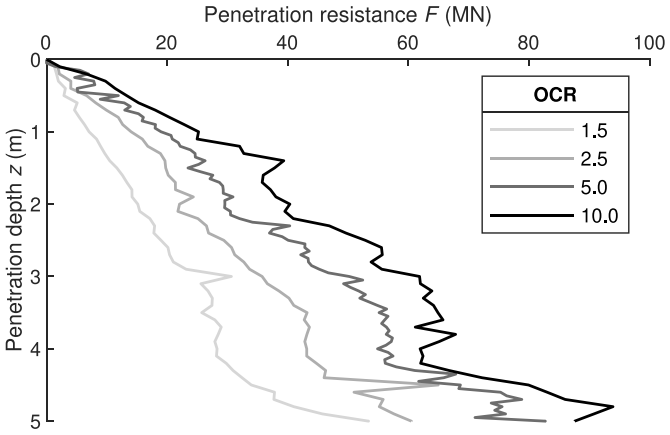

Fig. 20. Penetration as a function of penetration depth with varying OCR.

less than vertical stiffness, $\alpha > 1$ indicates greater horizontal than vertical stiffness, and $\alpha = 1$ corresponds to isotropic stiffness conditions. Fig. 18 shows the void ratio distribution in the soil before and after pile penetration, below the initial ground surface. The soil has been compacted both within and around the pile. When comparing isotropic stiffness conditions ($\alpha = 1$) with anisotropic stiffness ($\alpha = 1.5$), only minor differences in void ratio are observed. This is likely due to the dominance of vertical loading during pile penetration, which primarily induces vertical strains. Since varying α alters only the horizontal stiffness while the vertical stiffness remains constant, the overall compaction behaviour is not strongly affected. Nevertheless, slightly more pronounced compaction can be identified in the anisotropic case, which is consistent with the increased horizontal confinement. These trends in void ratio correspond well with the horizontal stress distributions shown in the magnified views in Fig. 18.

Fig. 19 demonstrates how penetration resistance F and vertical displacement z vary with changes in α. The simulations show that penetration resistance slightly increases with higher α reflecting the expected rise in horizontal stiffness. However, the effect remains modest, as the penetration process is predominantly governed by vertical loading, and the soil's vertical stiffness is unaffected by changes in α.

Fig. 20 presents the simulation results for OCR ranging from 1.5 to 10, plotted as pile resistance versus vertical pile displacement. The results show a clear increase in soil resistance when transitioning from the normally consolidated state (OCR = 1) to overconsolidated states (OCR > 1). This trend is consistent with expectations, as overconsolidated soils typically exhibit reduced compressibility and enhanced shear strength. Overall, the applied AVISA model captures the characteristic behaviour of fine-grained soils, realistically reflecting the decrease in compressibility and the increase in shear strength with rising OCR.

Further simulations were carried out for varying OCR and different pile outer diameters. The resulting normalised penetration resistances are plotted against penetration depth in Fig. 21. This representation facilitates the development of empirical approximations to characterise normalised penetration resistance across different pile geometries and OCR. The observed trends are well captured by the following function, which reflects the nonlinear increase in penetration resistance with depth:

$$\frac{F}{\gamma z_0 A_{\text{base}}} = 4.4\left(1 - e^{-5.95\frac{z}{D}^{0.69}}\right)\left(\frac{A_{\text{base}}}{D^2}\right)^{-0.74}\text{OCR}^{0.36}. \tag{8}$$

To avoid unrealistically large values when the pile tip is located near the ground surface, a reference depth z_0 is introduced in the

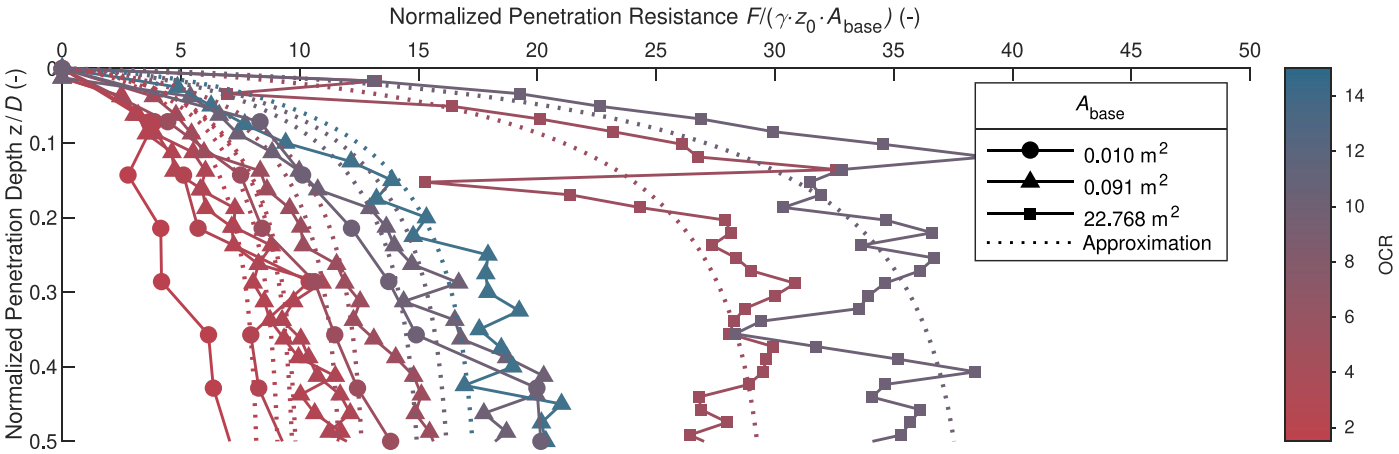

Fig. 21. Normalised penetration resistance versus penetration depth for varying OCR values.

normalisation. This ensures numerical stability and physical plausibility of the approximation across shallow and deep penetrations.

$$z_0 = 1\,\mathrm{m} + z \tag{9}$$

In summary, this section presented numerical LDFE CEL simulations of open-ended tubular pile penetration into Frankfurt clay. The results demonstrate significant influences of the surrounding soil conditions, particularly when comparing isotropic and anisotropic stiffness as well as varying OCR. While anisotropy exerted only a minor effect on pile resistance and void ratio, the impact of overconsolidation was substantial. Specifically, pile resistance increased by more than 100 % in highly overconsolidated soils, underscoring the necessity of accounting for OCR in penetration modelling.

6. Conclusion and outlook

The AVISA model has been successfully reformulated for explicit large deformation simulations, capturing both stiffness anisotropy and overconsolidation effects. Its performance was demonstrated in two applications: an explicit dynamic Lagrangian analysis of crane stability during uppercarriage rotation, and a CEL simulation of tubular pile penetration. In both cases, the simulation results showed good qualitative agreement with experimental data and analytical predictions, confirming the plausibility of the model. The AVISA model reliably reflects the increase in penetration resistance and construction machine stability associated with a higher horizontal stiffness and overconsolidation ratio. Moreover, the simulations enabled the derivation of simplified relationships linking system response to OCR and anisotropy, providing a valuable tool for preliminary design evaluations.

While the findings highlight the potential of the AVISA model, further laboratory and field investigations are planned to validate the model across a wider range of soil types and loading conditions. In particular, targeted cyclic loading experiments will help to evaluate AVISA's ability to capture both rate-dependent and rate-independent behaviour under repeated or dynamic loading in large deformation scenarios.

CRediT authorship contribution statement

D.A. Dao: Writing – review & editing, Writing – original draft, Visualization, Validation, Software, Project administration, Methodology, Investigation, Formal analysis, Data curation, Conceptualization. **M. Tafili:** Writing – review & editing, Writing – original draft, Visualization, Validation, Software, Project administration, Methodology, Investigation, Formal analysis, Data curation, Conceptualization. **F. Williams-Riquer:** Writing – review & editing, Writing – original draft, Visualization, Validation, Software, Methodology, Investigation, Formal analysis, Data curation, Conceptualization. **J. Grabe:** Writing – review & editing, Supervision, Resources, Funding acquisition. **T. Wichtmann:** Writing – review & editing, Writing – original draft, Supervision, Resources.

Declaration of competing interest

The authors declare the following financial interests/personal relationships which may be considered as potential competing interests: D.A. Dao reports financial support was provided by German Research Foundation. M. Tafili reports financial support was provided by German Research Foundation. F. Williams-Riquer reports financial support was provided by Federal Ministry for Economic Affairs and Climate Action. J. Grabe reports financial support was provided by German Research Foundation. T. Wichtmann reports financial support was provided by German Research Foundation. If there are other authors, they declare that they have no known competing financial interests or personal relationships that could have appeared to influence the work reported in this paper.

Acknowledgments

Duy Anh Dao, Francisco Williams-Riquer and Jürgen Grabe thank the Federal Ministry of Economic Affairs and Climate Action (BMWK) for funding the IGF project no. 20348N and the German Research Foundation (DFG) for their financial assistance, under Grant GR 1024/61-1. Merita Tafili and Torsten Wichtmann thank the DFG for the financial support in the framework of the project TR 218/29-1, TA 1696/1-1, WI 3180/9-1 as well as project no. 549595908 and 447999811.

Data availability

Data will be made available on request.

Nomenclature

Symbol/abbreviation	Explanation
A_{base}	Base surface area
AVISA	Anisotropic Visco ISA model
$c_b = f(\dot{\epsilon})$	Back-intergranular strain tensor
C_a	Accumulation rate factor
CEL	Coupled Eulerian–Lagrangian
D	Pile outer diameter
d_p	Penetration depth
e_{i0}	Reference void ratio
E	Young's modulus
E_{s}	Secant modulus
$\mathsf{E} = f(\boldsymbol{\sigma}, e)$	Transversal hypoelastic stiffness tensor
E_{v}	Young's modulus, vertical direction
EVF	Eulerian Volume Fraction
F	Penetration resistance
f_{b0}	Loading surface factor
FE	Finite Element
FEM	FE Method
$\mathbf{F}_{\text{h}} = 0$	Intergranular strain state
	on yield surface
	during plastic flow
G_{v}	Shear modulus, vertical direction
$h_{\text{b}} = f(\dot{\epsilon}, c_{\text{b}})$	Intergranular strain tensor
I_{v}	Viscosity index
IGA	Intergranular strain
ISA	Intergranular Strain Anisotropy
L	Length
LDFE	Large deformation FE (analysis)
L_{el}	Characteristic element length
$m = f(\sigma)$	Stress dependant flow rule
M_{c}	Critical state slope
MC	Mohr–Coulomb
m_{R}	Stiffness factor
n_{OCR}	Viscous exponent
OCR	Overconsolidation ratio
p'	Mean effective stress plane
p_{ref}	Reference pressure
q	Deviatoric stress
R	ISA yield surface radius
R	Pile resistance
RMSE	Root Mean Square Error
RP	Reference point
t	Pile wall thickness
t_0	Reference time

Symbol/abbreviation	Explanation
$\tan\frac{1}{3}\varphi_{\text{c}}$	Friction coefficient
$u_{z,A}$	Vertical displacement at point A
$u_{z,B}$	Vertical displacement at point B
$u_{z,C}$	Vertical displacement at point C
UMAT	User Material
VUMAT	Vectorised User Material
v_{max}	Maximum lateral velocity
v_{z}	Velocity
y_{h}	Scalar intergranular strain factor
Y	Degree of nonlinearity
z	Vertical displacement
z_0	Reference depth
α	Anisotropic coefficient
$\dot{\alpha}$	Stress rate tensor
β_0	ISA strain hardening parameter
γ	Unit weight
Δt_{crit}	Time step
ϵ	Strain
ϵ_a	Damage strain rate
$\dot{\epsilon}$	Total strain rate
$\dot{\epsilon}^{\text{hp}}$	Hypoplastic strain rate
$\dot{\epsilon}^{\text{vis}}$	Viscous strain rate
κ	Swelling index
λ	Compression index
λ_0	Minimum accumulation exponent
λ_{max}	Maximum accumulation exponent
ν	Poisson's ratio
ν_{h}	Poisson's ratio, horizontal direction
ρ	Unit weight
ρ_{s}	Dry unit weight
$\dot{\boldsymbol{\sigma}}$	Stress rate tensor
ϕ	Slewing angle
ϕ_{complete}	45 ° rotation of the uppercarriage
ϕ_{max}	Maximum uppercarriage rotation
φ	Internal friction angle
φ_{c}	Critical friction angle
χ	Exponent
χ_0	Minimum exponent
χ_{max}	Maximum exponent
ψ_1	Tilt
ψ_2	Roll
w_{L}	Liquid limit
w_{P}	Plastic limit

References

Aguiar, S.C.D., Modaressi-Farahmand-Razavi, A., dos Santos, J., Lopez-Caballero, F., 2011. Elastoplastic constitutive modelling of soil-structure interfaces under monotonic and cyclic loading. Comput. Geotech. 38, 430–447. http://dx.doi.org/10.1016/j.compgeo.2011.02.006.

Andersen, K.H., Dyvik, R., Schrøder, K., Hansteen, O.E., Bysveen, S., 1993. Field tests of anchors in clay II: Predictions and interpretation. J. Geotech. Eng. 119 (10), 1532–1549.

Arnold, M., Herle, I., 2006. Hypoplastic description of the frictional behaviour of contacts. In: Schweiger, H. (Ed.), Proceedings of the 6th European Conference on Numerical Methods in Geotechnical Engineering. pp. 101–106. http://dx.doi.org/10.1201/9781439833766.ch14.

Bai, Y., Guo, P., Lin, H., Liang, R., Yuan, B., Wang, Y., 2024. Penetration mechanism of open-ended pipe piles under jacking and driving methods. Mech. Adv. Mater. Struct. 1–20. http://dx.doi.org/10.1080/15376494.2024.2387746.

Bathe, K.J., 2006. Finite Element Procedures.

Benson, D.J., 1992. Computational methods in Lagrangian and Eulerian hydrocodes. Comput. Methods Appl. Mech. Engrg. 99 (2), 235–394. http://dx.doi.org/10.1016/0045-7825(92)90042-I.

Bienen, B., Fan, S., Schröder, M., Randolph, M.F., 2021. Effect of the installation process on monopile lateral response. Proc. Inst. Civ. Eng. - Geotech. Eng. 174 (5), 530–548. http://dx.doi.org/10.1680/jgeen.20.00219.

Bienen, B., Stanier, S., Vulpe, C., Mašín, D., 2014. Interface enabling constitutive models coded as user materials to be employed in explicit analysis. Reserach Rep. 14756, Reserach report.

BS EN 16228-1, 2021. Drilling and foundation equipment. Safety. Common requirements. Standard. British Standards Institution.

Carter, J.P., 2024. Constitutive modelling in computational geomechanics – 61st rankine lecture, British geotechnical association, 2023. Géotechnique 74 (13), 1511–1535.

Construction Plant-hire Association, 2014. Good practice guide - ground conditions for construction plant. URL: https://cpa.uk.net/downloads/110/SFPSG-Guidance-on-Ground-Conditions-Published-Document-with-logos.pdf.

Dafalias, Y.F., Manzari, M.T., Papadimitriou, A.G., 2006. SANICLAY: simple anisotropic clay plasticity model. Int. J. Numer. Anal. Methods Geomech. 30 (12), 1231–1257.

Dao, D., Alkateeb, D., Schröder, M., 2023. Discrepancies between element tests and large-scale LDFE simulations: A case study on anchor kinematics during installation in clay. Comput. Geotech. 163, 105698. http://dx.doi.org/10.1016/j.compgeo.2023.105698.

Dao, D.A., Dicke, K., 2022. Numerical investigation of drag embedment anchor model reduction for FOWTs in coarse and fine-grained baltic sea soil. In: Proceedings

of the 5th International Conference on Geotechnics for Sustainable Infrastructure Development. Hanoi, Vietnam, pp. 2871–2886. http://dx.doi.org/10.1007/978-981-99-9722-0_199.

Dao, D.A., Grabe, J., 2022. Numerical investigation of ship anchor penetration in cohesive baltic sea soil. In: 41st International Conference on Ocean, Offshore and Arctic Engineering (OMAE 2022). American Society of Mechanical Engineers, Hamburg, Germany, http://dx.doi.org/10.1115/OMAE2022-80822, V009T10A002.

Dao, D.A., Grabe, J., Tafili, M., Wichtmann, T., 2025. Simulation großer verschiebungen bei pfählen in anisotropen und überkonsolidierten feinkörnigen böden. In: Pfahl-Symposium 2025. Braunschweig, Germany.

Dao, D.A., Tafili, M., Grabe, J., Wichtmann, T., 2024. Simulation of large displacements during pile installation in anisotropic cohesive soil. In: GeoMontréal 2024: 77th Canadian Geotechnical Conference and the 16th Joint CGS/IAH-CNC Groundwater Conference. Montréal, Canada.

Dassault Systèmes, 2025a. ABAQUS Analysis User's Manual: Section 1.2.2 Conventions. Dassault Systèmes, Available with the ABAQUS software documentation.

Dassault Systèmes, 2025b. ABAQUS User Subroutines Reference Manual: Section 1.2.4 VUMAT User Subroutine to Define Material Behavior. Dassault Systèmes, Available with the ABAQUS software documentation.

Dejaloud, H., Rezania, M., 2021. Adaptive anisotropic constitutive modeling of natural clays. Int. J. Numer. Anal. Methods Geomech. 45 (12), 1756–1790.

Doherty, P., Gavin, K., 2011. Shaft capacity of open-ended piles in clay. J. Geotech. Geoenvironmental Eng. 137 (11), 1090–1102. http://dx.doi.org/10.1061/(asce)gt.1943-5606.0000528.

Doherty, P., Gavin, K., Gallagher, D., 2010. Field investigation of base resistance of pipe piles in clay. Proc. Inst. Civ. Eng. - Geotech. Eng. 163 (1), 13–22. http://dx.doi.org/10.1680/geng.2010.163.1.13.

Duque, J., Tafili, M., Seidalinov, G., Mašín, D., Fuentes, W., 2022. Inspection of four advanced constitutive models for fine-grained soils under monotonic and cyclic loading. Acta Geotech. 17 (10), 4395–4418.

Duriez, J., Vincens, F., 2015. Constitutive modelling of cohesionless soils and interfaces with various internal states: An elasto-plastic approach. Comput. Geotech. 63, 33–45. http://dx.doi.org/10.1016/j.compgeo.2014.08.001.

Edwards, D.J., Holt, G.D., 2010. Case study analysis of construction excavator H&S overturn incidents. Eng. Constr. Archit. Manag. 17 (5), 493–511. http://dx.doi.org/10.1108/09699981011074583.

Fakharian, K., Evgin, E., 2000. Elasto-plastic modelling of stress-path dependent behaviour of interfaces. Int. J. Numer. Anal. Methods Geomech. 24 (2), 183–199. http://dx.doi.org/10.1002/(SICI)1096-9853(200002)24:2<183::AID-NAG63>3.0.CO;2-3.

Fourie, A.B., Potts, D.M., 1991. A numerical and experimental study of London clay subjected to passive stress relief. Géotechnique 41 (1), 1–15.

Fuentes, W., Mašín, D., Duque, J., 2021. Constitutive model for monotonic and cyclic loading on anisotropic clays. Géotechnique 71 (8), 657–673.

Fuentes, W., Tafili, M., Triantafyllidis, T., 2018. An ISA-plasticity-based model for viscous and non-viscous clays. Acta Geotech. 13, 367–386.

Fuentes, W., Triantafyllidis, T., 2015. ISA model: a constitutive model for soils with yield surface in the intergranular strain space. Int. J. Numer. Anal. Methods Geomech. 39 (11), 1235–1254.

Grabe, J., Dao, D.A., 2024. Modeling the interaction between ship anchors and cables in baltic sea soils. In: Proceedings of the 17th Pan-American Conference on Soil Mechanics and Geotechnical Engineering. La Serena, Chile.

Graham, J., Houlsby, G., 1983. Anisotropic elasticity of a natural clay. Géotechnique 33, 165–180. http://dx.doi.org/10.1680/geot.1983.33.2.165.

Gylland, A.S., Jostad, H.P., Nordal, S., 2014. Experimental study of strain localization in sensitive clays. Acta Geotech. 9, 227–240.

He, Y.Q., Liao, H.J., Wu, W., Wang, S., 2023. Hypoplastic modeling of inherent anisotropy in normally and overconsolidated clays. Acta Geotech. 18 (12), 6315–6333.

Hossain, M., O'Loughlin, C., Kim, Y., 2015. Dynamic installation and monotonic pullout of a torpedo anchor in calcareous silt. Géotechnique 65 (2), 77–90. http://dx.doi.org/10.1680/geot.13.P.153.

Hu, L., Pu, J., 2003. Application of damage model for soil-structure interface. Comput. Geotech. 30, 165–183. http://dx.doi.org/10.1016/S0266-352X(02)00059-9.

Kargar, V., Jahangiri, M., Alimohammadlu, M., Kamalinia, M., Mirazahossieninejad, M., 2022. Risk assessment of mobile crane overturning in asymmetric tandem lifting (ATL) operation based on fuzzy fault tree analysis (FFTA). Results Eng. 16 (100755), 100755. http://dx.doi.org/10.1016/j.rineng.2022.100755.

Keller, T., Arvidsson, J., 2016. A model for prediction of vertical stress distribution near the soil surface below rubber-tracked undercarriage systems fitted on agricultural vehicles. Soil Tillage Res. 155, 116–123. http://dx.doi.org/10.1016/j.still.2015.07.014.

Lascarro, C., Ochoa-Cornejo, F., Mercado, V., Duque, J., 2024. An extended hypoplastic model for sands with additions of highly plastic fines formulated under the ISA framework. Soil Dyn. Earthq. Eng. 176, 108348.

Li, W., Islam, N., Deng, L., 2023. Large deformation finite element analyses of axially loaded helical piles in cohesive soil. Comput. Geotech. 164, 105819. http://dx.doi.org/10.1016/j.compgeo.2023.105819.

Liu, W., Shi, M., Miao, L., Xu, L., Zhang, D., 2013. Constitutive modeling of the destructuration and anisotropy of natural soft clay. Comput. Geotech. 51, 24–41.

Liu, J., Zou, D., Kong, X., 2014. A three-dimensional state-dependent model of soil-structure interface for monotonic and cyclic loadings. Comput. Geotech. 61, 166–177. http://dx.doi.org/10.1016/j.compgeo.2014.05.012.

Mašín, D., 2014. Clay hypoplasticity model including stiffness anisotropy. Géotechnique 64 (3), 232–238.

Mašín, D., Rott, J., 2014. Small strain stiffness anisotropy of natural sedimentary clays: review and a model. Acta Geotech. 9, 299–312.

Medicus, G., Tafili, M., Bode, M., Fellin, W., Wichtmann, T., 2023. Clay hypoplasticity coupled with small-strain approaches for complex cyclic loading. Acta Geotech. 1–20.

Miranda, P., Vargas Jr., E., Moraes, A., 2020. Evaluation of the modified cam clay model in basin and petroleum system modeling (BPSM) loading conditions. Mar. Pet. Geol. 112, 104112.

Mita, K., Dasari, G., Lo, K., 2004. Performance of a three-dimensional Hvorslev–modified cam clay model for overconsolidated clay. Int. J. Geomech. 4 (4), 296–309.

Moormann, C., Worbes, R., Lerner, T., 2018. Tragschichten für Arbeitsplattformen von mobilen Baumaschinen und Kranaufstellflächen. Technical Report, Universität Stuttgart.

Niemunis, A., Herle, I., 1997. Hypoplastic model for cohesionless soils with elastic strain range. Mech. Cohesive- Frict. Mater.: An Int. J. Exp. Model. Comput. Mater. Struct. 2 (4), 279–299.

Noh, W., 1963. CEL: A Time-Dependent, Two-Space-Dimensional, Coupled Eulerian-Lagrange Code. Lawrence Radiation Laboratory, http://dx.doi.org/10.2172/4621975.

Rafai, M., Tafili, M., Dong, Y., Vardon, P., 2025. Thermo-plastic analyses of energy pile in soft soils. (submitted for publication).

Rødvand, L.A., Jostad, H.P., Grimstad, G., Andresen, L., 2023. Modelling mesh independent failure loads of a soft strain-softening clay using a rate dependent model. Comput. Geotech. 161, 105512.

Roscoe, K., Burland, J.B., 1968. On the generalized stress-strain behaviour of wet clay.

Ross, B., McDonald, B., Vijay Saraf, S., 2007. Big blue goes down. The miller park crane accident. Eng. Fail. Anal. 14 (6), 942–961. http://dx.doi.org/10.1016/j.engfailanal.2006.12.002.

Song, Q., Zhang, T., Zhou, G., Li, H., Li, X., Jiang, Y., Zhao, P., Tian, W., Wang, Y., Zhang, C., Liu, H., 2022. Laboratory tests on open-close pile jacking and load bearing characteristics in saturated clay soil. In: Aloisio, A. (Ed.), Adv. Civ. Eng. 2022 (1), http://dx.doi.org/10.1155/2022/1369171.

Stapelfeldt, M., Alkateeb, D., Grabe, J., Bienen, B., 2020. Numerical simulation of cone penetration tests inside suction caisson foundations in sand. In: 39th International Conference on Ocean, Offshore and Arctic Engineering (OMAE 2020). American Society of Mechanical Engineers, http://dx.doi.org/10.1115/OMAE2020-18721, V010T10A007.

Staubach, P., Machaček, J., Tafili, M., Wichtmann, T., 2022. A high-cycle accumulation model for clay and its application to monopile foundations. Acta Geotech. 17 (3), 677–698.

Staubach, P., Tschirschky, L., Machaček, J., Wichtmann, T., 2023. Monopile installation in clay and subsequent response to millions of lateral load cycles. Comput. Geotech. 155, 105221. http://dx.doi.org/10.1016/j.compgeo.2022.105221.

Stutz, H., Mašín, D., Sattari, A., Wuttke, F., 2017. A general approach to model interfaces using existing soil constitutive models: Application to hypoplasticity. Comput. Geotech. 87, 115–127. http://dx.doi.org/10.1016/j.compgeo.2017.02.010.

Tafili, M., 2024. REV-wincdr: understanding constitutive models in representative elementary volume. https://github.com/MeritaTafili/REV-wIncDr/tree/main. (Accessed 21 June 2025).

Tafili, M., 2025. Modeling temperature-and rate-dependent behavior of soft soils: A thermo-visco-hypoplastic approach. Int. J. Numer. Anal. Methods Geomech..

Tafili, M., Albared, A., Prada-Sarmiento, L.F., Wichtmann, T., 2023a. Loading rate influence on high-cyclic loading of clays. Soil Dyn. Earthq. Eng. 173, 108103.

Tafili, M., Dao, D.A., Grabe, J., Wichtmann, T., 2025. Simulation of large displacements during lateral pile loading in anisotropic, overconsolidated fine-grained soils. In: 5th International Symposium on Frontiers in Offshore Geotechnics. ISFOG, Nantes, France, http://dx.doi.org/10.53243/ISFOG2025-61.

Tafili, M., Duque, J., Mašín, D., Wichtmann, T., 2024a. A hypoplastic model for pre-and post-liquefaction analysis of sands. Comput. Geotech. 171, 106314.

Tafili, M., Duque, J., Mašín, D., Wichtmann, T., 2024b. Repercussion of overshooting effects on elemental and finite-element simulations. Int. J. Geomech. 24 (3), 06024001.

Tafili, M., Ganal, A., Wichtmann, T., Reul, O., 2023b. On the AVISA model for clay–recommendations for calibration and verification based on the back analysis of a piled raft. Comput. Geotech. 154, 105126.

Tafili, M., Grandas, C., Triantafyllidis, T., Wichtmann, T., 2022a. Constitutive anamnesis model (CAM) for fine-grained soils. Int. J. Numer. Anal. Methods Geomech. 46 (15), 2817–2848.

Tafili, M., Grandas Tavera, C., Triantafyllidis, T., Wichtmann, T., 2021a. On the dilatancy of fine-grained soils. Geotechnics 1 (1), 192–215.

Tafili, M., Medicus, G., Bode, M., Fellin, W., 2022b. Comparison of two small-strain concepts: ISA and intergranular strain applied to barodesy. Acta Geotech. 17 (10), 4333–4358.

Tafili, M., Staubach, P., Machaček, J., Zachert, H., Wichtmann, T., 2024c. Predictive abilities of constitutive models for clay under monotonic and cyclic loading: element tests and centrifuge experiments. Géotechnique 1–17.

Tafili, M., Triantafyllidis, T., 2019. State-dependent dilatancy of soils: experimental evidence and constitutive modeling. In: Recent Developments of Soil Mechanics and Geotechnics in Theory and Practice. Springer, pp. 54–84.

Tafili, M., Triantafyllidis, T., 2020a. AVISA: anisotropic visco-ISA model and its performance at cyclic loading. Acta Geotech. 15 (9), 2395–2413.

Tafili, M., Triantafyllidis, T., 2020b. A simple hypoplastic model with loading surface accounting for viscous and fabric effects of clays. Int. J. Numer. Anal. Methods Geomech. 44 (16), 2189–2215.

Tafili, M., Triantafyllidis, T., 2023. Cyclic and monotonic response of silts and clays: experimental analysis and constitutive modelling. Eur. J. Environ. Civ. Eng. 27 (6), 2303–2312.

Tafili, M., Wichtmann, T., Triantafyllidis, T., 2021b. Experimental investigation and constitutive modeling of the behaviour of highly plastic lower rhine clay under monotonic and cyclic loading. Can. Geotech. J. 58 (9), 1396–1410.

Urbański, A., Richter, M., 2021. Stability analysis of heavy machinery moving on weak subsoil. analytical solution. Eng. Struct. 241, 112152. http://dx.doi.org/10.1016/j.engstruct.2021.112152.

Wang, D., Bienen, B., 2016. Numerical investigation of penetration of a large-diameter footing into normally consolidated kaolin clay with a consolidation phase. Géotechnique 66 (11), 947–952. http://dx.doi.org/10.1680/jgeot.15.P.048.

Wang, Y., Sang, S., Zhang, M., Bai, X., Su, L., 2021. Investigation on in-situ test of penetration characteristics of open and closed PHC pipe piles. Soils Found. 61 (4), 960–973. http://dx.doi.org/10.1016/j.sandf.2021.06.003.

Wang, Y.Y., Sang, S.K., Zhang, M.Y., Jeng, D.S., Yuan, B.X., Chen, Z.X., 2022. Laboratory study on pile jacking resistance of jacked pile. Soil Dyn. Earthq. Eng. 154, 107070. http://dx.doi.org/10.1016/j.soildyn.2021.107070.

Wichtmann, T., Triantafyllidis, T., 2018. Monotonic and cyclic tests on kaolin: a database for the development, calibration and verification of constitutive models for cohesive soils with focus to cyclic loading. Acta Geotech. 13, 1103–1128.

Wiesenthal, P., Henke, S., 2024. Concept on plug development in jacked open-ended piles in clay considering total stresses. Acta Geotech. 20 (3), 1019–1033. http://dx.doi.org/10.1007/s11440-024-02455-0.

Wiesenthal, P., Henke, S., 2025. Numerical investigation of soil plugging in clay with the CEL method and effective contact stresses. In: 5th International Symposium on Frontiers in Offshore Geotechnics. ISFOG, Nantes, France, http://dx.doi.org/10.53243/ISFOG2025-112.

Williams Riquer, F., Dao, D.A., Grabe, J., 2022. Towards the development of a digital twin for subsoil monitoring and stability against overturning of a mobile drilling rig. http://dx.doi.org/10.22260/ISARC2022/0030.

Zdravković, L., Taborda, D.M., Potts, D.M., Abadias, D., Burd, H.J., Byrne, B.W., Gavin, K.G., Houlsby, G.T., Jardine, R.J., Martin, C.M., et al., 2020. Finite-element modelling of laterally loaded piles in a stiff glacial clay till at cowden. Géotechnique 70 (11), 999–1013.

Zhou, X., Lu, D., Zhang, Y., Du, X., Rabczuk, T., 2022. An open-source unconstrained stress updating algorithm for the modified Cam-Clay model. Comput. Methods Appl. Mech. Engrg. 390, 114356.

Zouain, N., Pontes, I., Vaunat, J., 2010. Potentials for the modified Cam-Clay model. Eur. J. Mech. A Solids 29 (3), 327–336.